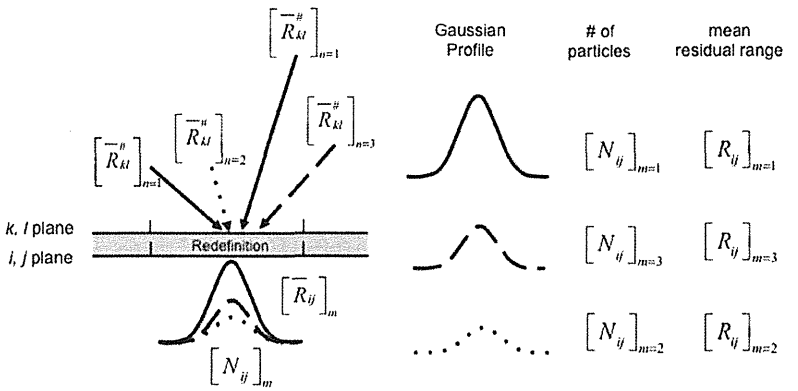

Figure 2. Illustration of the beam generation immediately after redefinition: Pencil beams with the residual range $(\overline{R}^{\#}_{kl})_n$ are transported to a calculation grid. The length of each arrow represents the number of particles. After redefinition, 'm' pencil beams are generated from the calculation grid. Area under the Gaussian profile represents the number of particles for the mth range bin $[N_{ij}]_m$. $[N_{ij}]_m$ and the mean residual range of the particles $[R_{ij}]_m$ in the patient plane $z = z_p$ are given in (8) and (9).

The number of particles for the mth range bin can be determined by summing the contribution from all of the range bins of the other pixels, as follows:

$$[N_{ij}(z_p)]_m = \sum_{k,l} [\Delta N^{\#}_{kl}]_m. \tag{8}$$

The mean residual range of the particles $[N_{ij}]_m$ in pixel (i, j, z_p) for the mth range bins is given by:

$$\begin{aligned}[\overline{R_{ij}}(z_p)]_m = \frac{1}{[N_{ij}(z_p)]_m} \sum_{k,l} \sum_{\substack{n=1 \\ \in R_m \leqslant (\overline{R}^{\#}_{kl})_n < R_{m+1}}}^{R_b} & \left(\overline{R}^{\#}_{kl}\right)_n \cdot (N^{\#}_{kl})_n \\ \times \frac{1}{2}\left[\operatorname{erf}\left(\frac{(\Delta x^{\#})_n + \frac{\delta_{xy}}{2}}{\sqrt{2\left(\overline{t^2}^{\#}_{kl}\right)_n}}\right) - \operatorname{erf}\left(\frac{(\Delta x^{\#})_n - \frac{\delta_{xy}}{2}}{\sqrt{2\left(\overline{t^2}^{\#}_{kl}\right)_n}}\right)\right] \\ \times \frac{1}{2}\left[\operatorname{erf}\left(\frac{(\Delta y^{\#})_n + \frac{\delta_{xy}}{2}}{\sqrt{2\left(\overline{t^2}^{\#}_{kl}\right)_n}}\right) - \operatorname{erf}\left(\frac{(\Delta y^{\#})_n - \frac{\delta_{xy}}{2}}{\sqrt{2\left(\overline{t^2}^{\#}_{kl}\right)_n}}\right)\right].\end{aligned} \tag{9}$$

As a result of the redefinition, the mth PBs (the total number of which is represented by R_b) are generated from pixel (i, j, z_p) (see figure 2).

As described in the appendix, other statistical and phase-space parameters of the redefined beam on the z_p plane for the mth range bin may be calculated in the same manner, by using the equations defined by Kanematsu *et al* (2008).

2.1.4. Dose deposition. The total dose distribution $D(x, y)$ at a given depth in the patient is given as follows:

$$D(x, y) = \sum_{i,j} \sum_{m=1}^{R_b} \frac{(N_{ij})_m (C_{ij})_m}{2\pi\left(\overline{t^2}_{ij}\right)_m} \exp\left(-\frac{(\Delta x)^2_m + (\Delta y)^2_m}{2\left(\overline{t^2}_{ij}\right)_m}\right) \tag{10}$$

where C_{ij} is the central-axis term of the dose distribution of a broad beam that was obtained in a water phantom, including an inverse square correction. The variables $(\Delta x)_m$ and $(\Delta y)_m$ are the distances between the PB axis for the mth range bin and the calculation grid. For practical calculation, the deposited dose of each calculation grid may be calculated by integrating over the calculation grid size, and (10) may be rewritten as follows:

$$D(x,y) = \sum_{kl}\sum_{m=1}^{R_b} (N_{kl})_m (C_{kl})_m \cdot \frac{1}{2}\left[\mathrm{erf}\left(\frac{(\Delta x)_m + \frac{\delta_{xy}}{2}}{\sqrt{2\left(\overline{t^2}_{kl}\right)_m}}\right) - \mathrm{erf}\left(\frac{(\Delta x)_m - \frac{\delta_{xy}}{2}}{\sqrt{2\left(\overline{t^2}_{kl}\right)_m}}\right)\right] \times \frac{1}{2}\left[\mathrm{erf}\left(\frac{(\Delta y)_m + \frac{\delta_{xy}}{2}}{\sqrt{2\left(\overline{t^2}_{kl}\right)_m}}\right) - \mathrm{erf}\left(\frac{(\Delta y)_m - \frac{\delta_{xy}}{2}}{\sqrt{2\left(\overline{t^2}_{kl}\right)_m}}\right)\right]. \quad (11)$$

2.2. *Experimental geometry*

The AVF cyclotron at the National Cancer Centre East (NCCE), Japan, accelerates protons to 235 MeV (Nishio 1999, Tachikawa *et al* 1999). In this study, laterally uniform dose distributions were obtained by the double-ring dual-scattered method (Nishio *et al* 2006). The PBA (Hong *et al* 1996, Szymanowski *et al* 2001) and the PBRA were analysed by comparing the calculation results with the measured proton dose distributions in a heterogeneous slab phantom and an anthropomorphic phantom. The PBA and PBRA calculations were executed on a 2.8 GHz Quad Core Intel Xeon processor. A PTW 2D Array seven29^{TM} (PTW, Freiburg, Germany) was used as a proton dose detector (Spezi *et al* 2005, Hotta *et al* 2010). This 2D detector matrix has 729 uniformly arranged ionization chambers in a 1.0 cm pitch 27 × 27 array. The sensitive volume of a unit chamber is 0.5 cm × 0.5 cm × 0.5 cm. The ionization chambers of the array are open to the air. The offset thickness from the entrance surface to the centre of the sensitive volume is 0.8 cm in water-equivalent thickness. To compare the calculation results and measurements under the same conditions, the depth calculation was corrected by the offset thickness for calculating the dose distributions.

In the PBRA calculation, the width of the range bin for the redefinition procedure was set to 0.2 cm, which corresponded to the calculation grid size. The calculation results were convolved with a detector cell size of 0.5 cm × 0.5 cm. For practical use, we also accelerated the PBRA calculation by GPU implementation. We adopted the CUDA platform (NVIDIA, Driver Version 4.2) for the GPU implementation. The calculations used Quadro 4000, which has 256 processor cores with a core clock rate of 950 MHz, and were based on a Fermi architecture.

2.2.1. Heterogeneous slab phantom. As shown in figure 3, a heterogeneous slab phantom was used in the measurement to examine an extreme case of lateral heterogeneity in a human body.

Although this phantom geometry is not found clinically, the configurations may elucidate the effects of lateral density heterogeneity of protons on dose distributions (Kohno *et al* 2003, Kanematsu *et al* 2009b, Hotta *et al* 2010, Egashira *et al* 2012). Monoenergetic 190 MeV proton beams were used, and the lateral dose distributions were measured at depths of $z = -9.2$ cm, -0.8 cm, 4.2 cm, and 6.1 cm, with various polyethylene plate thicknesses. The air gap between the rectangular aperture of 10.0 cm × 10.0 cm and the phantom

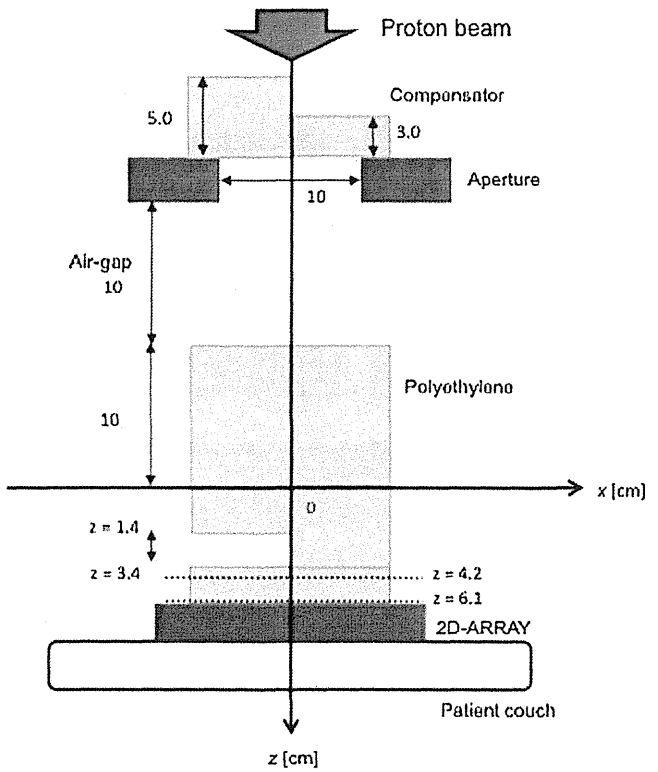

Figure 3. Experimental geometry for a heterogeneous slab phantom.

surface was fixed at 10.0 cm. The chamber pitch of 2D detector matrix we used was 1.0 cm. Since we were interested in the dose distribution close to the Bragg peak, the detector was shifted by 0.5 cm in the x direction to merge measurements with a lateral sampling pitch of 0.5 cm in the measurement at depths of $z = 4.2$ cm, and 6.1 cm. In the PBRA calculation, the interval of the redefinition planes was set equal to that of the calculation grids. For comparing the measurements and calculations, all of the dose data sets were normalized at a point ($x = -3.0$ cm, $y = 0.0$ cm, $z = -9.2$ cm) in the flat dose region. The computing time was monitored for the PBA and PBRA methods.

2.2.2. *Anthropomorphic phantom.* In the clinical situation, protons pass through complicated structures in the human body. To simulate the complicated arrangement of materials experienced in clinical applications, the head portion from a RANDO® phantom (Phantom Laboratory) was used. The calculated results were compared with measured data obtained by Hotta *et al* (2010). In this section, we briefly explain the experimental situation.

The anthropomorphic phantom mimics the density distribution in the human head by using resins with various compositions. Figure 4 shows the median sagittal and horizontal computed tomography (CT) images and the planning target volume (PTV) for this phantom, assuming a head and neck cancer with a volume of approximately 500 cm^3. The phantom was

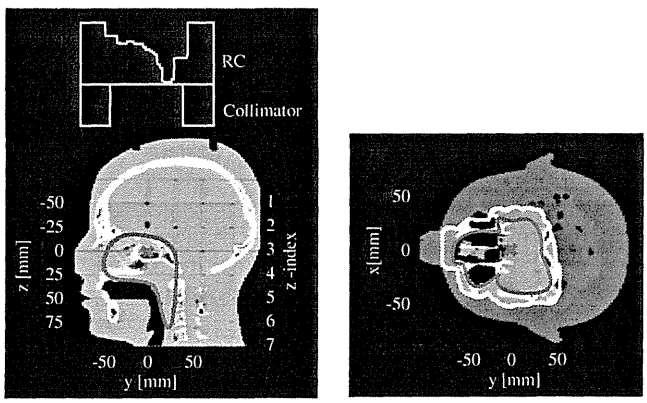

Figure 4. Experimental geometry for the anthropomorphic phantom measured by Hotta *et al* (2010).

composed of 2.5 cm thick horizontal layers. Dose distributions were measured in layers with Z-indices ranging from 1 to 7, which corresponded to $z = -50$ mm to $z = 100$ mm.

To simulate the clinical situation, the actual patient treatment procedure was performed, as follows: CT images were obtained, the PTV was delineated, the beam direction was determined, the corresponding range compensator and aperture collimator were manufactured, reference surface markers on the phantom were aligned with laser cross-hairs, and the phantom was irradiated on the patient couch. The smearing distance of the range compensator (Kooy *et al* 2008) was taken as 0.45 cm. A 235 MeV proton beam was modulated with a spread-out Bragg peak width of 6.0 cm, and a stack of phantom layers was mounted on the detector to measure the dose distribution in each measurement plane. The distance between the aperture collimator and the phantom entrance surface was fixed by adjusting the couch height. The reported results are the average of three measurements. All of the dose data sets were normalized with reference to the dose at the isocentre. The computing time was monitored for the PBA and PBRA methods.

3. Results

3.1. Heterogeneous slab phantom

The PBRA calculation was evaluated with the heterogeneity slab phantom. Figure 5 compares the depth- and lateral-dose profiles obtained from measurements and from the PBA and PBRA calculations.

As shown in figure 5(a), the main and overshot Bragg peaks appeared near depths of $z = 4$ cm and $z = 6$ cm, respectively. Lateral-dose profiles are shown in figures 5(b)–(e) at phantom depths of $z = -9.2$ cm, $z = -0.8$ cm, $z = 4.2$ cm and $z = 6.1$ cm, respectively. The PBRA was clearly superior to the conventional PBA in predicting the dose distribution in the region just distal to and shadowed by the edges of the inhomogeneity (air/polyethylene), particularly at the cold and hot spots. Although the magnitude of differences between the PBRA and measurements was as much as 2% at $z = 4.2$ cm, the geometry was very sensitive to misalignment of the density interface between the range compensator and the heterogeneous

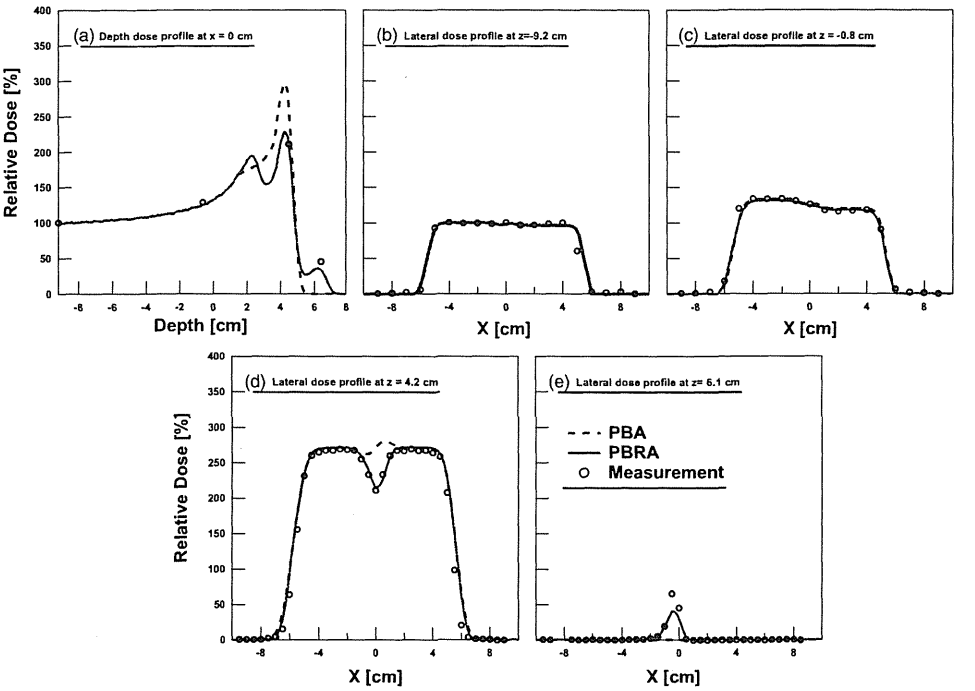

Figure 5. Depth- and lateral-dose distributions for the heterogeneous slab phantom.

slab in the phantom. The computational times for the PBA, PBRA and GPU-based PBRA calculations were 9.21, 60.2 and 30.1 s, respectively (see figure 8).

3.2. Anthropomorphic phantom

The PBRA calculation was evaluated with the anthropomorphic phantom. Figure 6 describes the isodose distributions in the coronal and sagittal planes at the isocentre obtained with the PBA calculation (left) and the PBRA calculation (right). The depth–dose distribution at $y = 0$ is also shown. The $Z = 6$ and $Z = 7$ planes were ignored because almost no protons reached these levels.

In the depth–dose profiles, discrepancies were observed between measurements and calculations and between the PBA and PBRA calculations. The discrepancy between measurements and calculations was caused by the range uncertainty of the phantom and the large dose gradient in the distal fall-off part of the Bragg curve. In the region that was deeper than $Z = 4$, where the protons reached the oral cavity, the difference between the PBA and PBRA calculations was more than 10%, due to differences in the path of the PB.

Figures 7(a) and (b) show the isodose distributions in the axial plane at the isocentre obtained with the PBA calculation (left), PBRA calculation (centre), and measurements (right) at $Z = 4$ and $Z = 5$. Lateral-dose profiles are also displayed in the figure, to illustrate some local differences.

The difference between the PBA and PBRA calculations arose from dose underestimations in the deep regions beyond air/tissue interface by the PBA, which disregarded the dose contributions of protons as they travelled through irregular paths along the phantom and reached the deep region. The distance to agreement (DTA) of the profiles around $x = 4$ cm

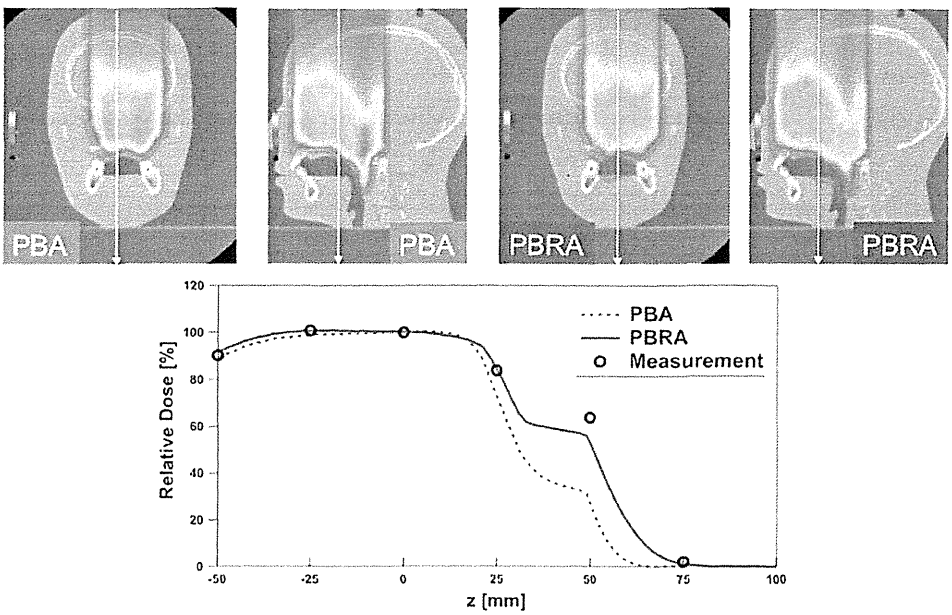

Figure 6. Isodose distributions in the coronal and sagittal planes and depth–dose distribution along the isocentre (arrow on the isodose distributions).

at $Z = 4$ and $y = 4$ cm at $Z = 5$, which were computed at a single point, were within 5 and 3 mm for the PBA and the PBRA calculations, respectively. The computational times for the PBA, PBRA and GPU-based PBRA calculations were 19.6, 272 and 59.0 s, respectively (see figure 8).

4. Discussion

This study addressed the use of the PBRA calculation in heterogeneous materials for proton therapy. Results calculated with the PBRA or PBA were compared with measured results in a heterogeneous slab phantom and an anthropomorphic phantom. The heterogeneous slab phantom simulated a simple geometry, in which an area of extreme lateral density heterogeneity was inserted. This set-up allowed us to investigate the effect of lateral density heterogeneity on the protons (Kohno *et al* 2003, Kanematsu *et al* 2009b, Hotta *et al* 2010, Egashira *et al* 2012). Behind the edges of the lateral density heterogeneity (i.e. air cavity), the dose was increased inside the edges and decreased outside, as more protons were scattered out by the polyethylene than were scattered in by the air cavity. The resulting detouring of the protons appeared as characteristic regions in the dose profiles.

Egashira *et al* (2012) reported that spatial resampling (i.e. beam redefinition) should be implemented immediately upstream of the lateral heterogeneity. Their resampling technique improved the accuracy of the PB calculation employing 1D density scaling because the number of the lateral heterogeneities in the compensator and phantom incidentally corresponded to the number of redefinition planes. As in Egashira *et al* (2012), we reconfirmed that use of the PBRA, in which the interval between and the number of redefinition planes may be arbitrary determined, also improved the accuracy of the proton PB calculation in this extreme geometry.

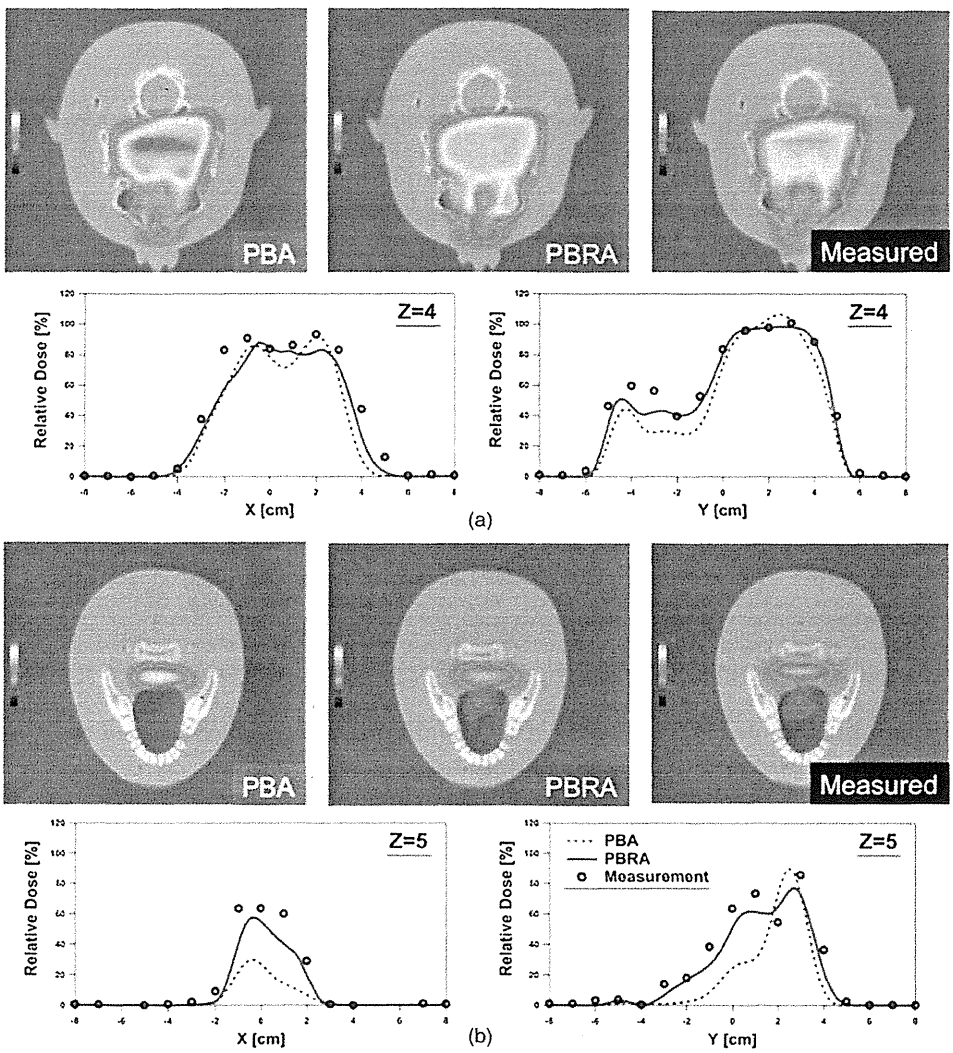

Figure 7. Isodose distributions in the axial plane and lateral-dose distribution in the x- and y-directions at (a) $Z = 4$ plane and (b) $Z = 5$ plane.

In clinical situations, protons pass through complicated structures, such as soft tissue, bone, and air, before they are stopped. To simulate this geometry, we used an anthropomorphic phantom with the measured data from Hotta *et al* (2010). In that previous study, the particles in the anthropomorphic phantom showed detouring effects due to multiple Coulomb scattering and nonstraight trajectories. The PBA disregarded the dose contributions of protons that travelled through irregular paths and reached the deep region and, therefore, underestimated the dose in the deep region (see figures 6 and 7). On the other hand, the redefined beams of the PBRA formed a detouring path that was different from PBs without redefinition, and the path of each redefined beam was straight. Consequently, the PBRA showed a dose increment

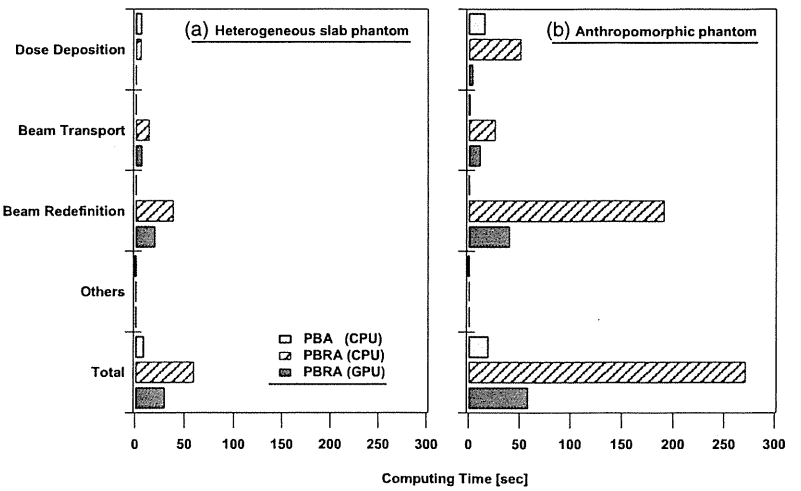

Figure 8. Performance of the PBA and PBRA calculations for the (a) heterogeneous slab phantom and (b) anthropomorphic phantom.

around depth $Z = 5$ on the depth–dose distribution along the isocentre, whereas the dose increment obtained by the PBA calculation was 51% lower than the measured increment (see figure 6).

Figure 9 compares the dose–area histograms obtained from the measurements and the PBA and PBRA calculations in each measurement plane.

The PBRA calculation was superior to the PBA, which underestimated the dose in deeper regions. The difference in calculation accuracy between the two algorithms arose from the consideration or disregard of irregular proton paths in heterogeneous media. The dose underestimation observed in the $Z = 4$ and $Z = 5$ planes even by the PBRA was caused by uncertainty in the CT value-to-range conversion and by the large low-density region. The doses in these regions are very sensitive to small uncertainties in the proton range because most protons in these regions have a small residual range. The reason for the large dose difference seen in the large dose gradient area is not well understood, but may be attributed to a lack of sufficient lateral scatter, which could be a result of a limitation of the redefinition process.

The trade-off between the calculation accuracy and computing time is often a significant factor in treatment planning. The computing time of the PBRA calculation was increased by the number of range bins, Rb (see m-loop in (11)), which depends on the complexity of the simulated geometry. For example, in the heterogeneous slab phantom, the number of range bins was up to three, owing to the L-shaped range compensator and the lateral heterogeneity (polyethylene/air). On the other hand, in the anthropomorphic phantom, up to 70 range bins were required for the PBRA calculation because of the complicated geometry. In the PBRA calculation, the slowing factors relative to the PBA calculation were 6.5 and 13.6 for the heterogeneity slab phantom and the anthropomorphic phantom, respectively. As shown in figure 8, the acceleration factors of the GPU-based acceleration of the PBRA calculation relative to the CPU-based PBRA calculation were 2.0 and 4.6 for the heterogeneity slab phantom and the anthropomorphic phantom, respectively. Fujimoto *et al* (2011) also found that GPUs were effective for implementing the PBA calculation. They observed 5–20 times faster performance using the NVIDIA Geforce GTX 480 card as compared to the Intel Core-i7

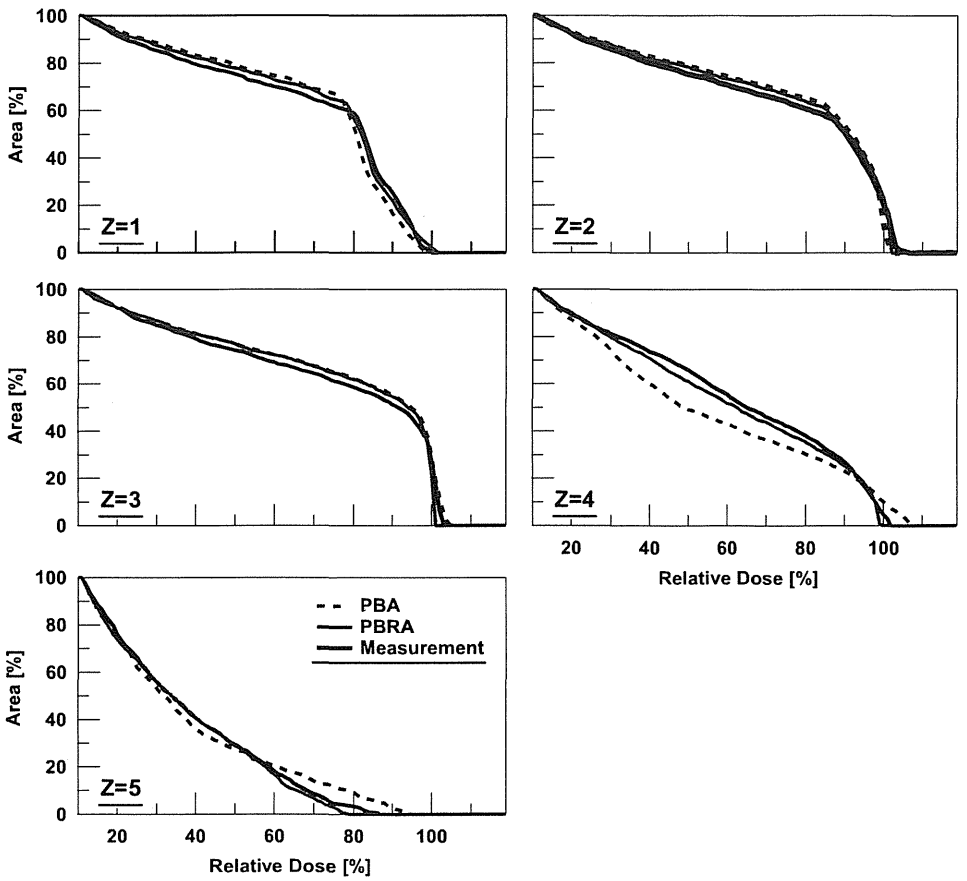

Figure 9. Dose–area histogram (DAH) at each measured plane.

920 processor. Their PBA, which employed 1D density scaling, used invariant dose kernelling, such that the data of the spatial variance of PB and the depth–dose distribution along the central axis of each PB could be stored in the GPU global memory before execution. In contrast, we used the Fermi–Eyges theory, in which the physics parameters were calculated and stored in the GPU global memory at each calculation plane. Because data transport between random access memory and GPU global memory can be a bottleneck of the GPU acceleration process (NVIDIA 2010), use of fewer accesses between the CPUs and GPUs may further accelerate the GPU-based PBRA calculation. Nevertheless, by the use of GPU implementation, dose calculation and optimization would help to reduce the clinical workload substantially in proton beam therapy.

5. Conclusions

The PBRA was applied to proton therapy to address the problem of lateral density heterogeneity. We addressed the problem of lateral density heterogeneity, by comparing the calculation results to dose distributions measured at different depths in a heterogeneous slab

phantom and an anthropomorphic phantom with a 2D detector. In the PBRA calculation, the redefined beams formed a detouring path that was different from the PBs without redefinition, and the path of each redefined beam was straight. Consequently, the PBRA was able to predict the measured proton-detouring effects. The GPU implementation of the PBRA achieved a speed-up factor of up to 4.6 relative to the PBRA calculation by CPU.

We conclude that the PBRA may improve the accuracy of PB calculation in heterogeneous media not only for electron therapy but also for proton therapy. The PBRA for protons requires more computational processes and longer computing time. However, by the use of GPU implementation, dose calculation and optimization would help to reduce the clinical workload substantially.

Acknowledgments

The authors would like to express their thanks to other members of the Medical Physics Group at NCCEH for their warm support and useful discussions. They also wish to thank SHI Accelerator Service, Ltd., for their help with measurements at the proton therapy facilities at the National Cancer Centre, Kashiwa. This work was partly supported by Health and Labour Science Research Grants from the Japanese Government. In addition, YE received a grant from the Japan Society for the Promotion of Science for Young Scientists as a Research Fellow of the Japan Society for the Promotion of Science.

Appendix. Statistical and phase-space parameters of the redefined beam

Statistical and phase-space parameters of the redefined beam on the z_p plane for mth range bin other than the number of particles $(N_{ij})_m$ and the mean residual range $(\overline{R}_{ij})_m$ are calculated in the same manner as the equation defined by Kanematsu *et al* (2008). The central axis position and the mean slopes of the redefined PBs are redefined at a patient plane $z = z_p$ as follows:

$$\left[\overline{x_{\mathrm{axis}ij}}\right]_m = x_j(z_p),\ \left[\overline{y_{\mathrm{axis}ij}}\right]_m = y_i(z_p) \tag{A.1}$$

$$\left[\overline{a_{xij}}(z_p)\right]_m = \frac{1}{[N_{ij}(z_p)]_m}\sum_{kl}\sum_{\substack{n=1 \\ \in R_m \leqslant (R_{kl}^{\#})_n < R_{m+1}}}^{R_b} \left(N_{kl}^{\#}\right)_n \cdot \mathrm{erfDiff}(y) \times \left\{\mathrm{erfDiff}(x)\cdot\left(\overline{a_{xkl}^{\#}}\right)_n - (A_{kl})_n \cdot \mathrm{expDiv}(x)\cdot \sinh \mathrm{Div}(x)\right\} \tag{A.2}$$

$$\left[\overline{a_{yij}}(z_p)\right]_m = \frac{1}{[N_{ij}(z_p)]_m}\sum_{k,l}\sum_{\substack{n=1 \\ \in R_m \leqslant (R_{i,j}^{\#})_n < R_{m+1}}}^{R_b} \left(N_{kl}^{\#}\right) \cdot \mathrm{erfDiff}(x) \times \left\{\mathrm{erfDiff}(y)\cdot\left(\overline{a_{ykj}^{\#}}\right)_n - (A_{kl})_n \cdot \mathrm{expDiv}(y)\cdot \sinh \mathrm{Div}(y)\right\}. \tag{A.3}$$

Any parameter p at the plane immediately before the device is denoted as $p^{\#} = p({}^{\#}z_p)$, where the PBs have not been redefined. erfDiff(x), expDiv(x), sinhDiv(x), coshDiv(x), $(A_{kl})_n$ appearing in the arguments of the function $\left[\overline{a_{xij}}(z_p)\right]_m$ and $\left[\overline{a_{yij}}(z_p)\right]_m$ are expressed as follows:

$$\mathrm{erfDiff}(x) \equiv \frac{1}{2}\left[\mathrm{erf}\left(\frac{(\Delta x^{\#})_n + \frac{\delta_{xy}}{2}}{\sqrt{2\left(\overline{t_{kl}^{2\#}}\right)_n}}\right) - \mathrm{erf}\left(\frac{(\Delta x^{\#})_n - \frac{\delta_{xy}}{2}}{\sqrt{2\left(\overline{t_{kl}^{2\#}}\right)_n}}\right)\right] \tag{A.4}$$

$$\mathrm{expDiv}(x) \equiv \exp\left(-\frac{(\Delta x^{\#})_n^2 + \frac{\delta_{xy}^2}{4}}{2\left(\overline{t^2}_{kl}^{\#}\right)_n}\right) \tag{A.5}$$

$$\sinh \mathrm{Div}(x) \equiv \sinh\left(\frac{(\Delta x^{\#})_n}{2\left(\overline{t^2}_{kl}^{\#}\right)_n} \cdot \delta_{xy}\right) \tag{A.6}$$

$$\cosh \mathrm{Div}(x) \equiv \cosh\left(\frac{(\Delta x^{\#})_n}{2\left(\overline{t^2}_{kl}^{\#}\right)_n} \cdot \delta_{xy}\right) \tag{A.7}$$

$$(A_{kl})_n \equiv \sqrt{\frac{2}{\pi\left(\overline{t_{kl}^2}^{\#}\right)_n^2}} \cdot \left(\overline{\theta t_{kl}}^{\#}\right)_n. \tag{A.8}$$

Similarly, the spatial variance $\left(\overline{t^2}_{ij}\right)_m$, angular variance $\left(\overline{\theta^2}_{ij}\right)_m$, and angular-spatial covariance $\left(\overline{\theta t}_{ij}\right)_m$ of the particles (Kanematsu *et al* 2008) are redefined as follows:

$$\begin{aligned}\left[\overline{\theta^2}_{ij}(z_p)\right]_m = {} & \frac{1}{\left[N_{ij}(z_p)\right]_m} \sum_{kl} \sum_{\substack{n=1 \\ \epsilon R_m \leqslant (R_{kl}^{\#})_n < R_{m+1}}}^{R_b} \left(N_{kl}^{\#}\right)_n \\ & \times \left\{ \begin{array}{l} \mathrm{erfDiff}(x) \cdot \mathrm{erfDiff}(y) \cdot \left(\left(\overline{\theta^2}_{kl}^{\#}\right)_n + \frac{[\overline{a_x}_{kl}^{\#}]_n^2 + [\overline{a_y}_{kl}^{\#}]_n^2}{2}\right) \\ -(B_{kl})_n \cdot \mathrm{expDiv}(x) \cdot \mathrm{erfDiff}(y) \\ \times \left[[E_{kl}(x)]_n \cdot \sinh \mathrm{Div}(x) + (D_{kl})_n \cdot \frac{\delta_{xy}}{4} \cdot \cosh \mathrm{Div}(x)\right] \\ -(B_{kl})_n \cdot \mathrm{expDiv}(y) \cdot \mathrm{erfDiff}(x) \\ \times \left[[E_{kl}(y)]_n \cdot \sinh \mathrm{Div}(y) + (D_{kl})_n \cdot \frac{\delta_{xy}}{4} \cdot \cosh \mathrm{Div}(y)\right] \end{array} \right\} \\ & - \frac{[\overline{a_x}_{ij}(z_p)]_m^2 + [\overline{a_y}_{ij}(z_p)]_m^2}{2}\end{aligned} \tag{A.9}$$

$$\left[\overline{\theta t}_{ij}(z_p)\right]_m = \frac{\delta_{xy}^2}{12\left|z_p - z_{\mathrm{src}}\right|}, \quad \left[\overline{t^2}_{ij}(z_p)\right]_m = \frac{\delta_{xy}^2}{12}. \tag{A.10}$$

$(B_{kl})_n$, $(D_{kl})_n$, $[E_{kl}(x)]_n$ appearing in the arguments of the function $\left[\overline{\theta^2}_{ij}(z_p)\right]_m$ are expressed as follows:

$$(B_{kl})_n \equiv \frac{\left(\overline{\theta t_{kl}}^{\#}\right)_n}{\sqrt{2\pi\left(\overline{t^2}_{kl}^{\#}\right)_n}} \tag{A.11}$$

$$(D_{kl})_n \equiv \frac{\left(\overline{\theta^2}_{kl}^{\#}\right)_n}{\left(\overline{t^2}_{kl}^{\#}\right)_n} \tag{A.12}$$

$$[E_{kl}(x)]_n \equiv \left[\overline{a_p}_{kl}^{\#}\right]_n - \frac{(\Delta x^{\#})_n}{2\left(\overline{t^2}_{kl}^{\#}\right)_n} \cdot \left(\overline{\theta t_{kl}}^{\#}\right)_n. \tag{A.13}$$

References

Boyd R A, Hogstrom K R and Starkschall G 2001 Electron pencil-beam redefinition algorithm dose calculations in the presence of heterogeneities *Med. Phys.* **28** 2096–104

Egashira Y, Nishio T, Matsuura T, Kameoka S and Uesaka M 2012 Experimental evaluation of a spatial resampling technique to improve the accuracy of pencil-beam dose calculation in proton therapy *Med. Phys.* **39** 4104

Eyges L 1948 Multiple scattering with energy loss *Phys. Rev.* **74** 1534–5

Fujimoto R, Kurihara T and Nagamine Y 2011 GPU-based fast pencil beam algorithm for proton therapy *Phys. Med. Biol.* **56** 1319–28

Gottschalk B, Koehler A M, Schneider R J, Sisterson J M and Wagner M S 1993 Multiple Coulomb scattering of 160 MeV protons *Nucl. Instrum. Methods* B **74** 467–90

Hogstrom K R, Michael M D and Almond P R 1981 Electron beam dose calculations *Phys. Med. Biol.* **26** 446–60

Hollmark M, Uhrdin J, Dž B, Gudowska I and Brahme A 2004 Influence of multiple scattering and energy loss straggling on the absorbed dose distributions of therapeutic light ion beams: I. Analytical pencil beam model *Phys. Med. Biol.* **49** 3247–65

Hong L, Goitein M, Bucciolini M, Comiskey R, Gottschalk B, Rosenthal S, Serago C and Urie M 1996 A pencil beam algorithm for proton dose calculations *Phys. Med. Biol.* **41** 1305

Hotta K, Kohno R, Takada Y, Hara Y, Tansho R, Himukai T, Kameoka S, Matsuura T, Nishio T and Ogino T 2010 Improved dose-calculation accuracy in proton treatment planning using a simplified Monte Carlo method verified with three-dimensional measurements in an anthropomorphic phantom *Phys. Med. Biol.* **55** 3545–56

Kanematsu N 2009a Semi-empirical formulation of multiple scattering for the Gaussian beam model of heavy charged particles stopping in tissue-like matter *Phys. Med. Biol.* **54** N67–73

Kanematsu N, Komori M, Yonai S and Ishizaki A 2009b Dynamic splitting of Gaussian pencil beams in heterogeneity-correction algorithms for radiotherapy with heavy charged particles *Phys. Med. Biol.* **54** 2015–27

Kanematsu N, Yonai S, Ishizaki A and Torikoshi M 2008 Computational modelling of beam-customization devices for heavy-charged-particle radiotherapy *Phys. Med. Biol.* **53** 3113–27

Kohno R, Takada Y, Sakae T, Terunuma T, Matsumoto K, Nohtomi A and Matsuda H 2003 Experimental evaluation of validity of simplified Monte Carlo method in proton dose calculations *Phys. Med. Biol.* **48** 1277–88

Kooy H M, Trofimov A, Engelsman M and Smith A R 2008 *Treatment planning Proton and Charged Particle Radiotherapy* ed T F Delaney and H M Kooy (Philadelphia, PA: Williams & Wilkins) chapter 8 pp 70–107

Nishio T 1999 Present status and planning of facilities for proton and heavy ion cancer treatment in Japan—National Cancer Center *J. At. Energy Soc. Japan* **41** 1134–8

Nishio T, Kataoka S, Tachibana M, Matsumura M, Uzawa N, Saito H, Sasano T, Yamaguchi M and Ogino T 2006 Development of a simple control system for uniform proton dose distribution in a dual-ring double scattering method *Phys. Med. Biol.* **51** 1249–60

NVIDIA 2010 NVIDIA CUDA Programming Guide Santa Clara, CA http://developer.download.nvidia.com/compute/cuda/3_0/toolkit/docs/NVIDIA_CUDA_ProgrammingGuide.pdf

Petti P L 1992 Differential-pencil-beam dose calculations for charged particles *Med. Phys.* **19** 137–49

Russell K R, Grusell E and Montelius A 1995 Dose calculations in proton beams: range straggling corrections and energy scaling *Phys. Med. Biol.* **40** 1031–43

Russell K R, Isacsson U, Saxner M, Ahnesjöh A, Montelius A, Grusell E, Vallhagen Dahlgren C, Lorin S and Glimelius B 2000 Implementation of pencil kernel and depth penetration algorithms for treatment planning of proton beams *Phys. Med. Biol.* **45** 9–27

Schaffner B, Pedroni E and Lomax A 1999 Dose calculation models for proton treatment planning using a dynamic beam delivery system: an attempt to include density heterogeneity effects in the analytical dose calculation *Phys. Med. Biol.* **44** 27–41

Shiu A and Hogstrom K R 1991 Pencil-beam redefinition algorithm for electron dose distributions *Med. Phys.* **18** 7–18

Spezi E, Angelini A L, Romani F and Ferri A 2005 Characterization of a 2D ion chamber array for the verification of radiotherapy treatments *Phys. Med. Biol.* **50** 3361–73

Szymanowski H, Mazal A, nauraye C, Biensan S, Ferrand R, Murillo M C, Caneva S, Gaboriaud G and Rosenwald J C 2001 Experimental determination and verification of the parameters used in a proton pencil beam algorithm *Med. Phys.* **28** 975–87

Szymanoqski H and Oelfke U 2002 Two-dimensional pencil beam scaling: An improved proton dose algorithm for heterogeneous media *Phys. Med. Biol.* **47** 3313–30

Tachikawa T, Sato T, Ogino T and Nishio T 1999 Proton treatment devices at National Cancer Center (Kashiwa, Japan) *Radiat. Indust.* **84** 48–53

Experimental evaluation of a spatial resampling technique to improve the accuracy of pencil-beam dose calculation in proton therapy

Yusuke Egashira[a)]
Department of Bioengineering, Graduate School of Engineering, University of Tokyo, 2-11-16, Yayoi, Bunkyo-ku, Tokyo 113-8656, Japan and Japan Society for the Promotion of Science, Ichibancho 8, Chiyoda-ku, Tokyo 102-8472, Japan

Teiji Nishio
Particle Therapy Division, Research Center for Innovative Oncology, National Cancer Center, Kashiwa, 6-5-1 Kashiwanoha, Kashiwa-shi, Chiba 277-8577, Japan

Taeko Matsuura
Department of Applied Molecular-Imaging Physics, Graduate School of Medicine, Hokkaido University, Sapporo, Hokkaido 060-8638, Japan

Satoru Kameoka
Particle Therapy Division, Research Center for Innovative Oncology, National Cancer Center, Kashiwa, 6-5-1 Kashiwanoha, Kashiwa-shi, Chiba 277-8577, Japan

Mitsuru Uesaka
Department of Bioengineering, Graduate School of Engineering, University of Tokyo, 2-11-16, Yayoi, Bunkyo-ku, Tokyo 113-8656, Japan

(Received 27 October 2011; revised 16 April 2012; accepted for publication 15 May 2012; published 11 June 2012)

Purpose: In proton therapy, pencil-beam algorithms (PBAs) are the most widely used dose calculation methods. However, the PB calculations that employ one-dimensional density scaling neglect the effects of lateral density heterogeneity on the dose distributions, whereas some particles included in such pencil beams could overextend beyond the interface of the density heterogeneity. We have simplified a pencil-beam redefinition algorithm (PBRA), which was proposed for electron therapy, by a spatial resampling technique toward an application for proton therapy. The purpose of this study is to evaluate the calculation results of the spatial resampling technique in terms of lateral density heterogeneity by comparison with the dose distributions that were measured in heterogeneous slab phantoms.

Methods: The pencil beams are characterized for multiple residual-range (i.e., proton energy) bins. To simplify the PBRA, the given pencil beams are resampled on one or two transport planes, in which smaller sub-beams that are parallel to each other are generated. We addressed the problem of lateral density heterogeneity comparing the calculation results to the dose distributions measured at different depths in heterogeneous slab phantoms using a two-dimensional detector. Two heterogeneity slab phantoms, namely, phantoms A and B, were designed for the measurements and calculations. In phantom A, the heterogeneity slab was placed close to the surface. On the other hand, in phantom B, it was placed close to the Bragg peak in the mono-energetic proton beam.

Results: In measurements, lateral dose profiles showed a dose reduction and increment in the vicinity of $x = 0$ mm in both phantoms at depths $z = 142$ and 161 mm due to lateral particle disequilibrium. In phantom B, these dose reduction/increment effects were higher/lower, respectively, than those in phantom A. This is because a longer distance from the surface to the heterogeneous slab increases the strength of proton scattering. Sub-beams, which were generated from the resampling plane, formed a detouring/overextending path that was different from that of elemental pencil beams. Therefore, when the spatial resampling was implemented at the surface and immediately upstream of the lateral heterogeneity, the calculation could predict these dose reduction/increment effects. Without the resampling procedure, these dose reduction/increment effects could not be predicted in both phantoms owing to the blurring of the pencil beam. We found that the PBA with the spatial resampling technique predicted the dose reduction/increment at the dose profiles in both phantoms when the sampling plane was defined immediately upstream of the heterogeneous slab.

Conclusions: We have demonstrated the implementation of a spatial resampling technique for pencil-beam calculation to address the problem of lateral density heterogeneity. While further validation is required for clinical use, this study suggests that the spatial resampling technique can make a significant contribution to proton therapy. © *2012 American Association of Physicists in Medicine.* [http://dx.doi.org/10.1118/1.4722984]

Key words: proton therapy, treatment planning, dose calculation, pencil-beam algorithm

I. INTRODUCTION

Passive scattering proton therapy has been widely implemented in many proton therapy facilities around the world. In proton therapy, it is most important to concentrate and conform the proton dose distributions to the tumor by utilizing the Bragg peak. Pencil-beam algorithms (PBA; Refs. 1–11) have been the most commonly used dose calculation method for charged-particle radiation therapy. In the PBA by Hong *et al.*,[3] the accuracy of the PBA is guaranteed in homogeneous material with reasonable computing time. However, the PBA calculations that employ one-dimensional density scaling neglect the effects of lateral density heterogeneity on the dose distributions, whereas some particles included in such pencil beams could overextend beyond the interface of the density heterogeneity.

Several techniques for addressing the problem of lateral density heterogeneities have been introduced into the PBAs. In the PB calculations that employ one-dimensional density scaling, elemental pencil beams were split into subbeams, which are smaller than an elemental pencil beam.[5–8] Schaffner *et al.*[5,6] reduced the over-reaching of protons by splitting each scanning beam into small virtual pencil beams for dose calculation on the patient surface. In the pencil-beam splitting algorithm,[7,8] each pencil beam is dynamically split into smaller ones, up to 4 × 4 Gaussian near the lateral density interface. For efficient dose calculation, split pencil beams are densely set as necessary; otherwise, large pencil beams are sparsely set. Two-dimensional density scaling,[9] namely, scaling of the lateral proton fluence, of the PB calculation has also improved the calculation accuracy around lateral density heterogeneities. However, the problem of lateral density heterogeneity is not new, and has been approached to improve the dosimetric accuracy of the pencil-beam calculation for electron therapy.[11,12] For example, the Fermi-Eyges theory[10] has been applied to the PB calculation for electron therapy. The pencil-beam redefinition algorithm (PBRA; Refs. 11 and 12) handles the electron flow and energy at the calculation plane in accordance with this theory. For the dose calculation and beam transportation, three physical quantities were required. Fluence, mean direction, and rms spread about the mean direction are characterized for multiple energy bins for a given pencil beam. The width of energy bins, which is typically defined as 0.5–1.0 MeV, determines the spectrum of the electron energy. When 5.0 mm interval between the redefinitions was used, it required 10–20 times pencil-beam redefinition for a 9–20 MeV electron beam. Since the rms spread about the mean direction of electrons immediately after the redefinition is minimal, the PB redefinition calculation improved the accuracy of pencil-beam dose calculation for electrons in the presence of heterogeneity. A similar idea to the PBRA was applied to heavy particles for beam customization, in which particle flow in the transverse plane was considered in the absence of heterogeneity.[13] In the presence of lateral heterogeneities, however, the concept of the PBRA has not been evaluated for dose calculation in proton therapy.

In this paper, a spatial resampling technique for pencil-beam calculation (SRPBA) is described. The concept of the spatial resampling technique is simplification of the PBRA toward the application of proton therapy. Provided that the PBRA is implemented for clinical proton therapy with no modification, the resultant number of energy bins will considerably increase owing to the compensator and the range modulator. While electrons can be scattered through very large angles so that their path is considerably modified, protons scatter by a few degrees and follow an only slightly nonstraight path. With the spatial resampling technique, the pencil beams that are defined with multiple residual-range (i.e., proton energy) bins are resampled on one or two transport planes. In addition, the mean directions of resampled subbeams are defined as parallel to each other. As a consequence of the spatial resampling technique, the SRPBA can similarly address the problem of lateral density heterogeneity. The purpose of this study is to evaluate the spatial resampling technique in terms of lateral density heterogeneity by the measurements in heterogeneous slab phantoms.

II. MATERIALS AND METHODS

II.A. Pencil-beam algorithm

In the PBA by Hong *et al.*,[3] the full beam is represented by a set of elemental pencil beams as follows:

$$D_{\mathrm{PBA}}(x, y, z) = \iint dx'dy' \cdot \Phi_0(x', y') \times \frac{C(x', y', \mathrm{WEL}(x', y', z))}{2\pi\left[\sigma_{\mathrm{PBA}}(x', y'; z)\right]^2} \times \exp\left(-\frac{(x'-x)^2 + (y'-y)^2}{2\cdot\left[\sigma_{\mathrm{PBA}}(x', y'; z)\right]^2}\right), \quad (1)$$

$$\sigma^2_{\mathrm{PBA}}(x', y'; z) = \sigma^2_{\mathrm{line,PBA}} + \sigma^2_{\mathrm{comp,PBA}} + \sigma^2_{\mathrm{pt,PBA}}, \quad (2)$$

$$\sigma^2_{\mathrm{line,PBA}} = \sigma^2_{\mathrm{size}} \cdot \left(\frac{\mathrm{airgap} + z}{d_{\mathrm{bld}}}\right)^2, \quad (3)$$

$$\sigma^2_{\mathrm{comp,PBA}} = \left(\frac{t}{2} + \mathrm{airgap} + z\right)^2 \cdot \sigma^2_{\theta}, \quad (4)$$

where $\Phi_0(x, y)$ is the fluence of the open beam and the integration is over the beam area. $C(x', y', \mathrm{WEL}(x', y', z))$ is the central-axis term of the dose distributions of the pencil beam located at (x', y'), including an inverse square correction. $\mathrm{WEL}(x', y', z)$ corresponds to water-equivalent length from the source to the point of interest (x', y', z). σ_θ is the characteristic scattering angle of range compensator calculated with the Highland formula.[14,15] The origin of the z axis is set to the surface of a patient. The total Gaussian beam size (standard deviation), so-called Gaussian-sigma, is composed of three components: (i) the effective source size σ_{size}, (ii) spatial spread due to scattering of the range compensator σ_{comp}, and (iii) spatial spread due to multiple scattering within the patient σ_{pt}. $\sigma_{\mathrm{PBA}}(x, y; z)$ is obtained by adding in quadrature the contributions from (i) to (iii). d_{bld} is the distance from the source to the downstream face of the aperture collimator.

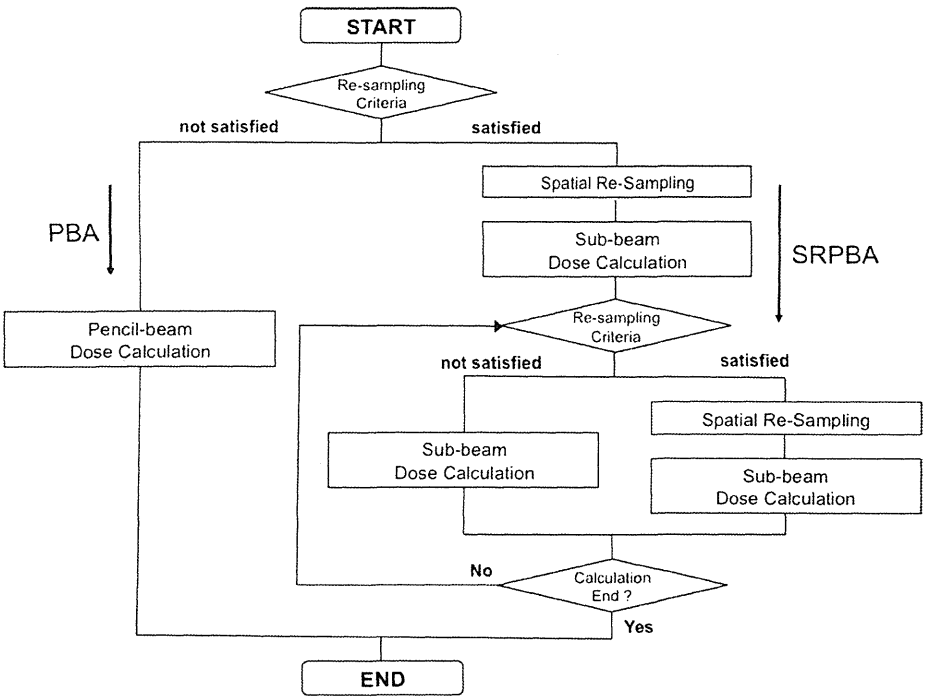

FIG. 1. Flow diagram of a spatial resampling technique for pencil-beam calculation (denoted as SRPBA). The resampling criteria (a) and (b) determine if pencil beams are resampled or not.

Airgap indicates the distance from the downstream face of the aperture collimator to the patient surface. t is the thickness of the range compensator.

II.B. Implementation of spatial resampling technique

The spatial resampling technique for pencil-beam calculation is the application of the PBRA proposed for electron beam therapy.[11,12] The PBRA requires three physical parameters, namely, fluence, mean direction, and spatial spread about the mean direction. The fluence is assumed to be uniform at the entrance to a range compensator and zero outside the aperture downstream of the range compensator. The mean direction of the protons for each elemental pencil beam emanated from the virtual source defines the direction of fan lines. The spatial spread about the mean direction for elemental pencil beams is obtained from Eq. (2). It is noteworthy that these physical quantities are characterized for multiple residual-range (i.e., proton energy) bins for given pencil beams.

Figure 1 shows a flow diagram of the spatial resampling procedure. For the calculation of protons, the number of redefinition planes could be reduced owing to a small scatter effect compared with that of electrons. Pencil beams generated at the entrance to the compensator are propagated to the patient surface including the effect of the scattering from the compensator and airgap from the downstream face of the aperture to the patient surface. The range modulator is treated as a set of degraders with weight factor.[16] The resampling procedure is implemented first at the patient surface with three physical parameters only when the spatial spread of the beams exceeds the calculation grid size. In other words, the first resampling criterion can be given as follows:

$$\sigma_{\mathrm{PBA}}(x', y'; z = 0) > \delta_{xy}, \tag{5}$$

where δ_{xy} is the grid size. Otherwise, if the first resampling criterion is not satisfied, the dose calculation by the other pencil beams follows the conventional one. For each range bin, at the resampling plane, the spatial spread of sub-beams is given by Eq. (A1) of Appendix A for each range bin. In addition, for simplification, the mean direction for all pencil beams is the same, and they are parallel to the beam axis. The sub-beam can be additionally resampled at an arbitrary plane, in which these beams satisfy the second criterion in terms of the fluence and the spatial spread to avoid unnecessary resampling. The secondary resampling criteria are given as follows:

$$\frac{[\Phi(x, y; z = 0)]_{R_{\mathrm{res}}(x,y;z=d_{\mathrm{smp}})}}{\sum_{R'=0}^{R_0}[\Phi(x, y; z = 0)]_{R'}} > \kappa_\Psi \quad \text{and}$$
$$\sigma_{\mathrm{SR_n}}(x, y; z = d_{\mathrm{smp}}) > \delta_{xy}, \tag{6}$$

where $[\Phi(x, y, ; z = 0)]_R$ is the fluence of the pencil beam per residual range R at the surface $(x, y, 0)$. $\sigma_{\mathrm{SR_n}}(x, y; d_{\mathrm{smp}})$ corresponds to the sigma of sub-beams at a depth of $z = d_{\mathrm{smp}}$ which is the secondary resampling depth. The parameters for these criteria $\sigma_{\mathrm{SR_n}}$ and $[\Phi(x, y, ; z = 0)]_R$ are given by Eqs. (A1) and (A6), respectively. R_0 is the initial residual range of pencil beam. To avoid the spatial resampling of the beams with a relatively small number of particles, the cutoff parameter κ_Ψ was chosen as 0.1. The number of resamplings is restricted to two: one at the surface plane and another inside the patient. All beams are propagated using one-dimensional density scaling until all protons are stopped. The relative dose

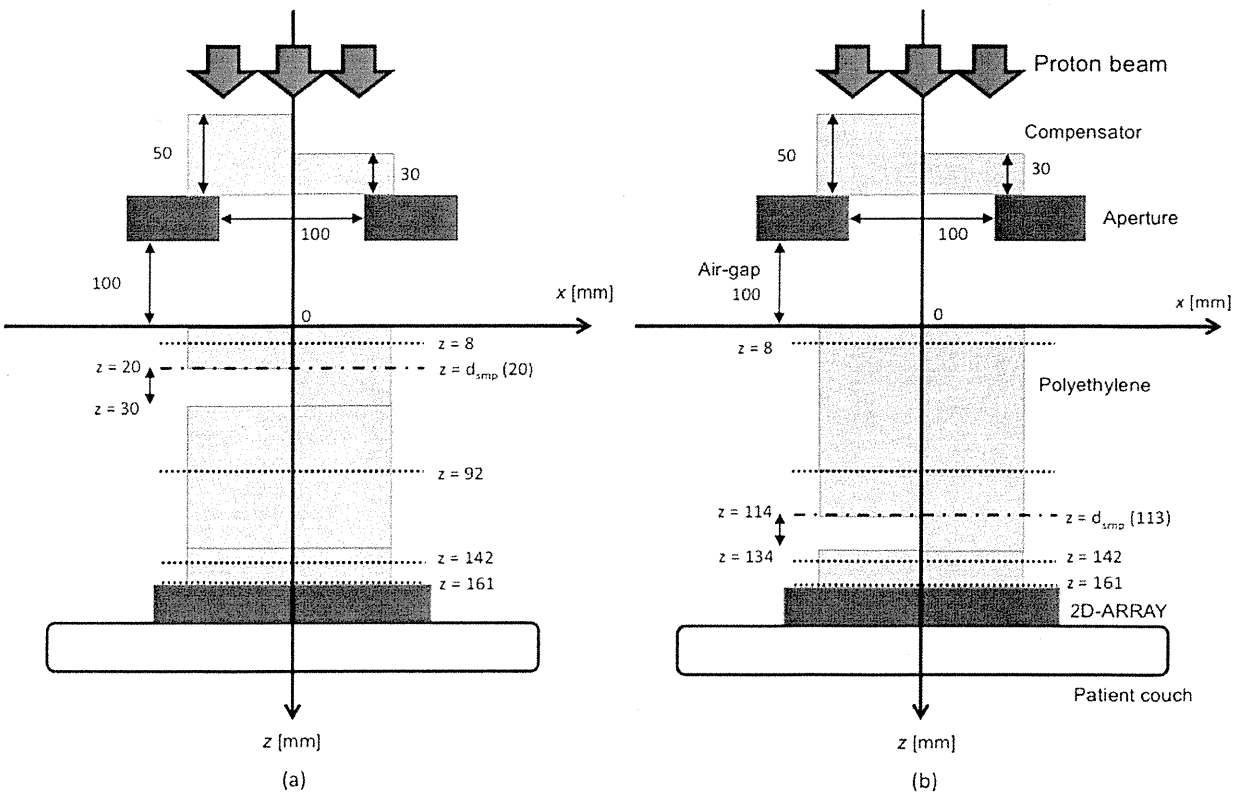

FIG. 2. Experimental arrangements for measurement. Polyethylene blocks were stacked as (a) phantom A and (b) phantom B. The dotted and dashed lines show the measurement and sampling planes, respectively.

for deposition in a patient voxel could be obtained from the measured depth-dose distributions in water. Details of the calculation of fluence and dose distributions are described in Appendix B. The spatial resampling technique for pencil-beam algorithm was implemented with 1 mm resolution using a 2.8 GHz Intel Core 2 Duo processor on an Apple iMac computer. In addition, the calculation result with this technique was compared to the conventional PBA described in Sec. II.A.

II.C. Beam line system and experimental geometry

At the National Cancer Center East (NCCE), Japan, 235 MeV protons accelerated by AVF cyclotron can be transported into three ports. For clinical use, two of the three ports have a rotating gantry, and the other has a horizontal fixed port.[17,18] In this study, 190 MeV proton beams were sent to the rotating gantry, and laterally uniform dose distributions were obtained by the dual-ring double-scattered method.[19]

We examined the PBA with or without the spatial resampling technique by comparing the calculation results with the experimentally measured dose distributions in heterogeneous slab phantoms. A PTW 2D Array seven29™ (PTW, Freiburg, Germany) was used as a proton dose detector.[20,21] This is a two-dimensional detector matrix with 729 uniformly arranged ionization chambers in a 10 mm pitch 27 × 27 array. The sensitive volume of a unit chamber is 5 mm × 5 mm × 5 mm. The ionization chambers of the array are open to the air. The offset thickness from the entrance surface to the center of the sensitive volume is 8 mm in water-equivalent thickness.[21] In order to compare the calculation results and measurements under the same conditions, we corrected the depth calculation by the offset thickness when calculating the dose distributions. We also convolved the calculation results with the detector cell size of 5 mm × 5 mm. The heterogeneous slab phantoms in Fig. 2 were used for verification of the spatial resampling technique. We investigated proton detouring and overextension effects, that is, lateral density heterogeneity effects, on dose distributions using a mono-energetic 190 MeV proton beam. As shown in the figure, two phantoms (A and B) were designed by stacking L-shaped polyethylene and polyethylene plates. The water-equivalent thickness of polyethylene was 1.02. In phantom A, the depth of the low-density region (air) was located at depths from $z = 30$ mm to 50 mm, which is the plateau of the depth-dose curve. On the other hand, in phantom B, the interface between air and polyethylene was located at depths from $z = 114$ mm to 134 mm, which is close to proton range. Lateral dose distributions were measured at depths of $z = 8$ mm, 92 mm, 142 mm, and 161 mm with changing thickness of the polyethylene plate. The air-gap between the rectangular aperture of 100 mm × 100 mm and the surface of the phantom was fixed at 100 mm. Since the chamber pitch was 10 mm, we shifted the detector by 5 mm in the x direction to merge measurements with a lateral sampling pitch of 5 mm. In the calculation, parallel pencil beams were generated at the entrance to the range

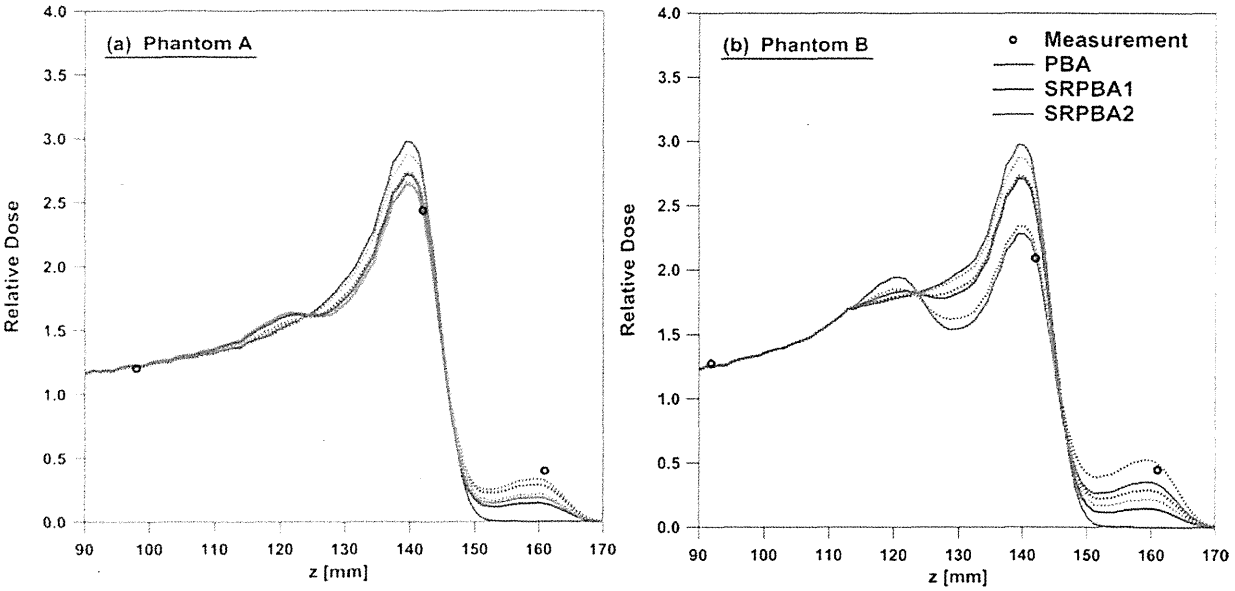

FIG. 3. Depth-dose profiles in (a) phantom A and (b) phantom B: Red, blue, and green solid lines depict calculation results using the PBA, the one with the resampling only at $z = 0$ (denoted as SRPBA1) and the one with the resampling at $z = 0$ and $z = d_{smp}$ (denoted as SRPBA2), respectively. Dashed lines depict calculation results considering 1 mm misalignment. In addition, open circle indicates measurements.

compensator because we are interested in the middle of the field, in which density interface was placed. With the spatial resampling technique implemented at $z = 0$ and $z = d_{smp}$, the depths of $d_{smp} = 30$ mm and 113 mm were chosen as those for secondary resampling in phantoms A and B, respectively. These depths correspond to those of the density interface between polyethylene and air in the phantoms. In order to consider the setup error of the phantom, all calculations were also carried out with 1 mm misaligned geometry from $x = 0$. All the dose data sets were normalized at a point ($x = -30$ mm, $y = 0$ mm, $z = 8$ mm) in a flat dose region for comparison of measurements and calculations.

III. RESULTS AND DISCUSSION

We addressed the problem of the lateral density heterogeneity comparing the calculation results to the dose distributions measured at different depths in heterogeneous slab phantoms using a two-dimensional detector. Figures 3 and 4 show comparisons of the depth and lateral dose profile obtained from measurements, the PB calculation with or without the spatial resampling technique. As shown in Fig. 3, the main and potential Bragg peaks appeared in the vicinity of the depths of $z = 140$ mm and $z = 160$ mm, respectively. Lateral dose profiles are shown in Figs. 4(a) and 4(b) at a depth of $z = 142$ mm of phantoms A and B, respectively. In measurements, both lateral dose profiles showed dose reduction in the vicinity of $x = 0$ mm owing to lateral particle disequilibrium.[23] As shown in Figs. 4(c) and 4(d), at a depth of $z = 161$ mm, both lateral dose profiles showed dose increment in the vicinity of $x = 0$ mm. When the spatial resampling was implemented, in phantom A, the minimal sub-beam could predict these dose reduction/increment effects. Without the resampling, the calculation could not reproduce these results because of the elemental pencil beams, which were substantially blurred by multiple Coulomb scattering. In phantom B, the calculation could predict these dose reduction/increment effects only when the spatial resampling was implemented at the surface and immediately upstream of the lateral heterogeneity. For quantitative evaluation of the accuracy in the density interface in the middle of the field, the difference of relative dose between $x = -25$ and 25 mm, which corresponds to half of the irradiation field, was calculated as follows:

$$\text{(Difference of relative dose)} = D_c(x) - D_m(x), \quad (-25 \le x \le 25 \text{ mm}), \tag{7}$$

where $D_c(x)$ and $D_m(x)$ are the calculated dose and the measured dose, respectively. Figure 5 shows a summary of the difference of relative dose. In summary, more resampling procedures improved the accuracy. In phantom A, the difference of relative dose of the PBA (without resampling), the PBA with resampling only at $z = 0$ and the PBA with resampling at $z = 0$ mm and $z = d_{smp}$ were within ± 0.48, ± 0.35, and ± 0.31, respectively. On the other hand, in phantom B, the relative dose difference of the PBA, the SRPBA (resampled at $z = 0$), and the SRPBA (resampled at $z = 0$ mm and $z = d_{smp}$) were within ± 0.65, ± 0.53, and ± 0.28, respectively. Without the spatial resampling, in phantom A, the calculation could not reproduce this dose reduction with $+10.7\%$ at $x = 0$ while the SRPBA could reproduce it within 1.5% when the setup error of 1 mm was taken into account. In phantom B, on the other hand, only the PBA with resampling at $z = 0$ and $z = d_{smp}$ could reproduce this dose reduction with 0.4% at $x = 0$ because the smaller size of resampled beam correctly predicted the lateral dose perturbation.

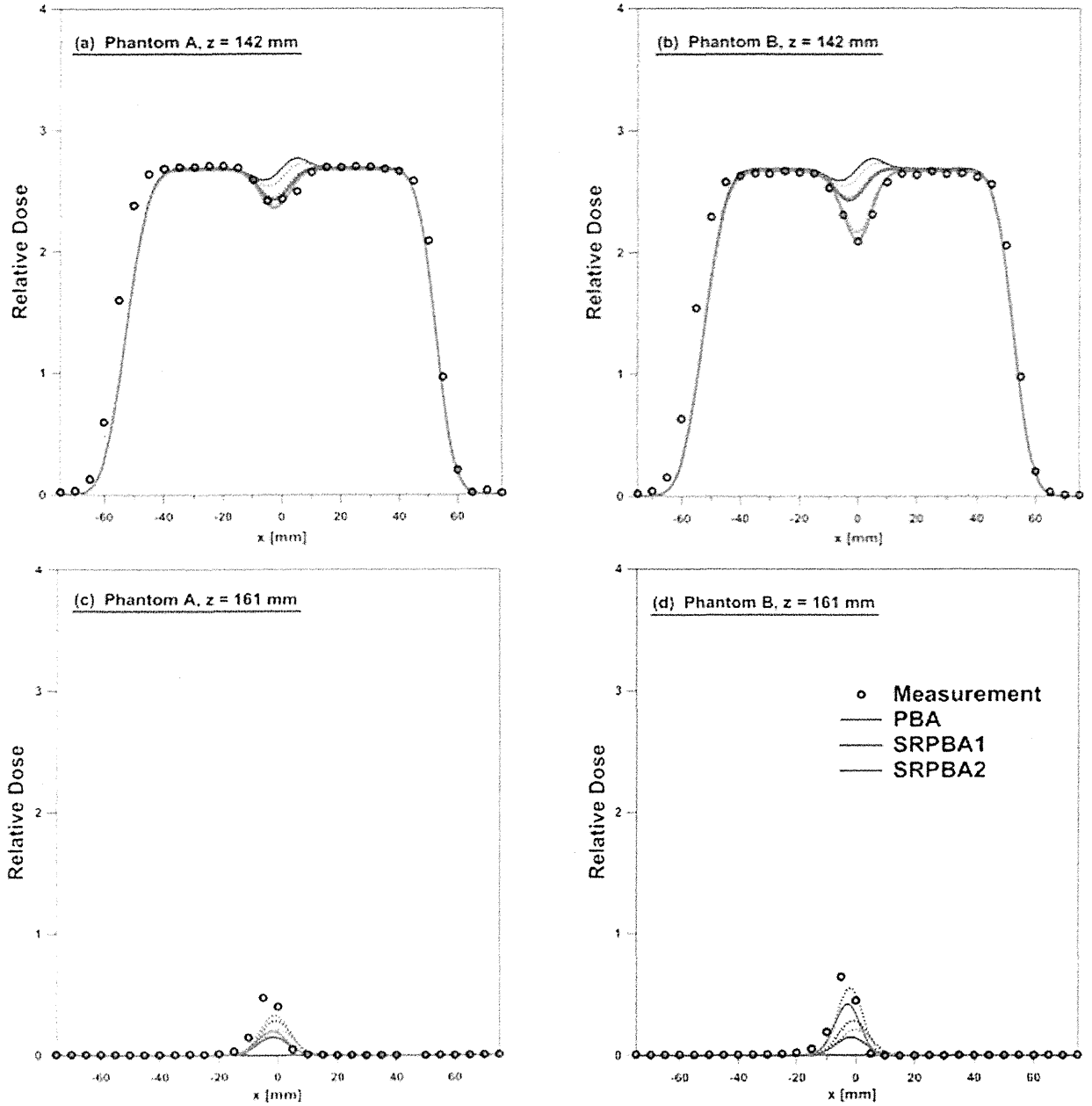

FIG. 4. Lateral dose profiles in the phantoms: Solid lines depict calculation results using the PBA, the one with the resampling only at $z = 0$ (denoted as SRPBA1) and the one with the resampling at $z = 0$ and $z = d_{\text{smp}}$ (denoted as SRPBA2). Dashed lines depict calculation results considering 1 mm misalignment. In addition, open circle indicates measurements.

While the experimental geometries that we used might be somewhat simple, they were effective for investigation of the lateral density heterogeneity effect of protons.[7,21,22] This is because the effect by the detouring/overextension of protons appeared as characteristic regions in the dose profiles. The geometry is illustrated in Fig. 6 for the case of phantom B of a parallel beam of protons impinging on two air/polyethylene interfaces in the range compensator and the heterogeneity slab phantom. The strength of multiple Coulomb scattering depends on the compensator thickness as given in Eq. (4). Therefore, the dose is primarily perturbed just below the range compensator (i.e., scattering-in and scattering-out of protons) owing to the difference of its thickness on sides 1 and 2. That is, as pointed out by Goitein,[23] protons on side 1 are more scattered by the compensator than on side 2. In the phantom, protons are transported to the density interface at $z = 114$ mm inside the phantom as they are scattered by polyethylene. A region such as A in Fig. 6 is traversed both by protons on side 1 and by some protons that came from side 2. Note that protons on side 1 and some protons that came from side 2 have

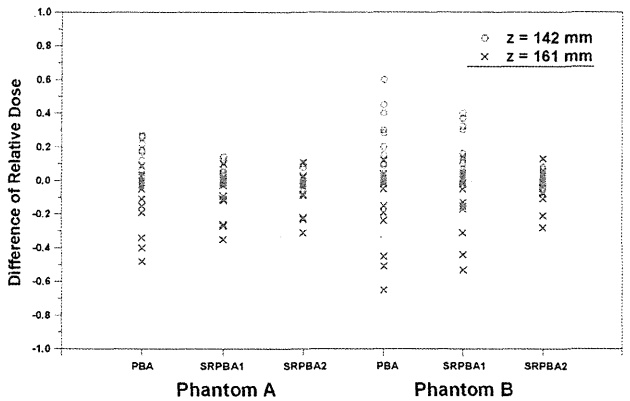

FIG. 5. Difference of relative dose between $x = -25$ and 25 mm: Calculation results which include the PBA, the one with the resampling only at $z = 0$ (denoted as SRPBA1) and the one with the resampling $z = 0$ and $z = d_{smp}$ (denoted as SRPBA2) minus measurements. Red open circle and blue cross depict the relative dose difference at depths $z = 142$ mm and $z = 161$ mm, respectively. The misalignment and nonmisalignment cases are merged in this figure.

different residual range (i.e., energy) due to the difference of the compensator thickness. In region B, the opposite occurs. Subsequently, protons from side 1 traverse the inhomogeneity (air), in which they are much less scattered than on side 2. Away from the density interface, the Bragg peak is formed around depth $z = 140$ mm. However, some protons from regions A and B, namely, detouring and overshooting protons, form Bragg peaks in the vicinity of $z = 120$ mm and 160 mm, respectively. Kanematsu *et al.*[7] and Hotta *et al.*[21] have reported the effect of detouring protons using similar geometry. Furthermore, we experimentally elucidated such effect on the proton dose distributions in the case that the depth of the inhomogeneous slab (air) was changed. The longer distance from the surface to the heterogeneous slab increased the strength of proton scattering. The number of protons from side 1 (or 2) at region B (or A) increased more in phantom B than in phantom A. In phantom B where the slab was placed in a deep region, therefore, this dose reduction was higher than that in phantom A where the slab was placed in a shallow region. For the same reason, the magnitude and the shape of the potential peak which were formed by the overshooting protons in phantom A were relatively small and spread compared with those in phantom B. Figure 7 shows the lateral dose profile at a depth of $z = 142$ mm, which corresponds to the main Bragg peak of phantom B. In the figure, the solid lines indicate the calculation results with changing of the secondary resampling depth from 14 mm to 113 mm. For comparison, the dose profile without spatial resampling is shown as well. Without the resampling procedure, the scattering-in and scattering-out effects of protons between sides 1 and 2 could not be predicted in the vicinity of the density heterogeneity owing to the blurring of pencil beams. In the calculation with the spatial resampling, sub-beams formed a detouring/overextension path that was different from elemental pencil beams, and predicted the lateral particle disequilibrium in the shadow of the

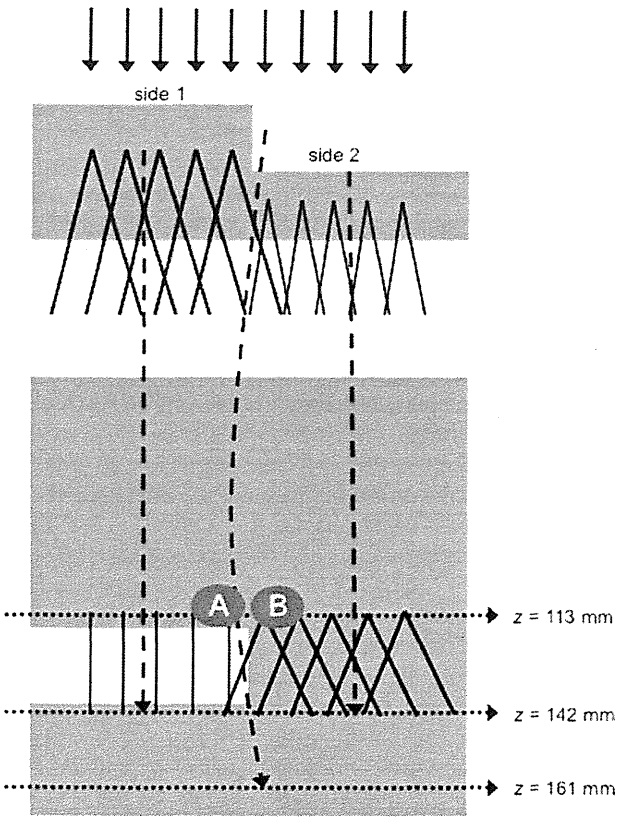

FIG. 6. Schematic drawing of an L-shaped compensator and phantom B intersecting a broad beam. Away from the interface between the two media (air /polyethylene), protons form the Bragg peak around depth $z = 142$ mm (dashed straight lines). On the other hand, close to the interface region such as A, protons are overextended (dashed curved line).

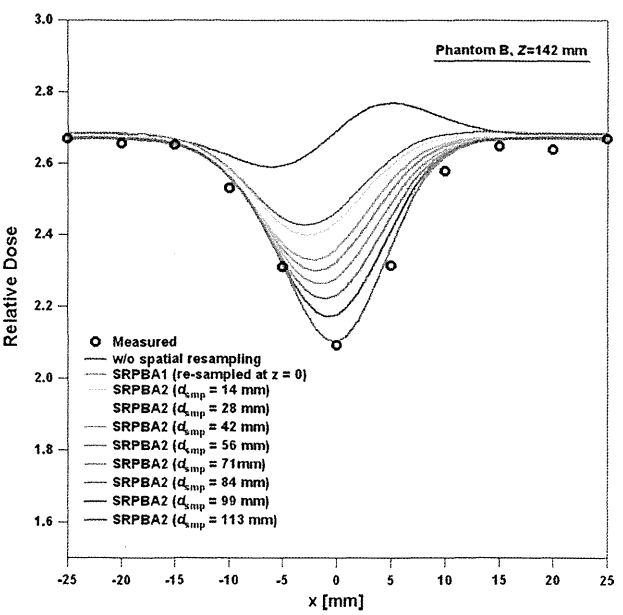

FIG. 7. Lateral dose profiles at $z = 142$ mm in phantom B upon changing the resampling depth of $z = d_{smp}$. Solid lines depict calculation results and open circles depict measurement data.

inhomogeneity. Thus, dose reduction and increment appeared in the lateral dose profiles of the calculation result by the spatial resampling. The accuracy of dose reduction adjacent to $x = 0$ mm was improved as the additional resampling depth was close to the heterogeneity interface. This is because proton disequilibrium shown in the dose profile was caused by the scattering from the compensator and the polyethylene from $z = 0$ mm to $z = 114$ mm. Therefore, the spatial resampling should be implemented immediately upstream of the lateral heterogeneity.

Indeed, in clinical situations, protons pass through more complicated structures such as soft tissue, bone, and air before they stop. These particles show detouring and overextension effects due to multiple Coulomb scattering, and their trajectories are not straight. Moreover, organs at risk often surround a target, especially in the head and neck region. In proton therapy with passive scattering method, the range spectra at the surface can be complicated due to the proton scattering from the range compensator. In this study, the number of range bins was up to two because of the L-shaped compensator and the simple lateral heterogeneity. The shape of the target and human heterogeneity determine the shape of the range compensator. Therefore, the complicated shape of the compensator and human heterogeneities increase the number of residual-range bins on the sampling plane.[24] In treatment planning, there are always trade-offs between accuracy and time. In the calculation of the spatial resampling for the H&N tumor, as described in Appendix C, the increases in computing time were by factors of 9 and 20 for one and two spatial resamplings, respectively, compared with the pencil-beam calculation without this technique. Although more resampling would improve the calculation accuracy for realistic radiotherapy applications, resampling more than three planes might be an extensive numerical task and less practical in the treatment planning process due to its time-consuming nature. The accuracy of the spatial resampling technique strongly depends on the secondary resampling depth while the setting at the appropriate depth improves the accuracy. An optimal way to choose d_{smp} may be determined by measurements in an anthropomorphic phantom or by Monte Carlo calculations for more realistic geometries. The number of residual-range bins also depends on the quantization level of the residual-range spectra. As future work, therefore, these parameters should be carefully set throughout the verification of many other realistic cases as future work. Also, a quantitative comparison between the SRPBA and the Schaffner *et al.* algorithm will be needed for a next step.

IV. CONCLUSIONS

We have demonstrated the implementation of the spatial resampling technique for pencil-beam calculation to approach the problem of lateral density heterogeneity in proton therapy. The PBRA that was proposed by Shiu and Hogstrom was simplified as the spatial resampling technique for proton therapy. In the calculation, the fluence was characterized for multiple residual-range (i.e., proton energy) bins for given pencil beams, and spatially resampled on one or two transport planes. We addressed the problem of lateral density heterogeneity comparing the calculation results to the dose distributions measured at different depths in heterogeneous slab phantoms using a two-dimensional detector. In the measurements of slab phantoms, we found that the spatial resampling technique for pencil-beam calculation reproduced the characteristic dose reduction/increment at the dose profiles when the sampling plane was defined immediately upstream of the heterogeneous slab. The spatial resampling technique could improve the accuracy of pencil-beam calculation using one-dimensional density scaling. While further validation is required for clinical use, this study suggests that the spatial resampling technique as the application of PBRA can make a significant contribution to proton therapy.

ACKNOWLEDGMENTS

The authors are grateful to Dr. Ryosuke Kohno and Dr. Kenji Hotta for useful discussions. They also wish to thank SHI Accelerator Service, Ltd., for their help with measurements at the proton therapy facilities at the National Cancer Center, Kashiwa. Y.E. received a grant from the Japan Society for the Promotion of Science for Young Scientists. This work was partly supported by Health and Labour Science Research Grants from the Japanese Government.

APPENDIX A: SPATIAL SPREAD OF SUB-BEAM

In this Appendix, we summarize the spatial spread of the sub-beam (i.e., pencil beam generated from the resampled planes). Like $\sigma_{\mathrm{PBA}}(z)$ shown in Eq. (2), the approximated Gaussian-sigma of sub-beam $\sigma_{\mathrm{SR}_n}(z)$ at arbitrary depth z is composed of three components,

$$\sigma^2_{\mathrm{SR}_n}(z) = \sigma^2_{\mathrm{line,SR}_n}(z) + \sigma^2_{\mathrm{comp,SR}_n}(z) + \sigma^2_{\mathrm{pt,SR}_n}(z). \quad \text{(A1)}$$

In the spatial resampling technique, we extended these terms as follows. From Eq. (3), we defined the following Gaussian-sigma $\sigma_{\mathrm{line,SR}_n}(z)$ with respect to the effective source size σ_{size} as follows:

$$\sigma^2_{\mathrm{line,SR}_n}(z) = \begin{cases} \{h(\mathrm{airgap})/z\} \cdot \sigma^2_{\mathrm{line,PBA}}(\mathrm{airgap} = 0) & (0 < z \le d_{\mathrm{smp}}), \\ \{(h(\mathrm{airgap}) + \eta \cdot g(\sigma_{\mathrm{size}}))/z\} \cdot \sigma^2_{\mathrm{line,PBA}}(\mathrm{airgap} = -d_{\mathrm{smp}}) & (z > d_{\mathrm{smp}}), \end{cases}$$
$$h(\mathrm{airgap}) = \alpha_1 \cdot \mathrm{airgap} + \beta_1,$$
$$g(\sigma_{\mathrm{size}}) = \alpha_2 \cdot \sigma^2_{\mathrm{size}} + \beta_2 \cdot \sigma_{\mathrm{size}} + \gamma_2, \quad \text{(A2)}$$

where R_0 is the residual range of the open beam. η is d_{smp}/R_0. The correction factors $h(\mathrm{airgap})$ and $g(\sigma_{\mathrm{size}})$ are required in order to minimize the difference between σ_{PBA} and σ_{SR} in air. On the basis of the nominal energies of protons of 150 MeV, 190 MeV,